Chapter 3
Collective Magnetic Behaviour

Roland Mathieu and Per Nordblad

Abstract The mechanisms responsible for magnetic interaction between nanoparticles are described and modelled in the previous chapter of this book. Here, the collective superspin glass state resulting from such interaction is discussed, using a collection of experimental results. Superspin glasses display qualitatively similar dynamical magnetic properties as canonical spin glasses, including ageing, memory and rejuvenation phenomena. In the Introduction, the dynamical properties of spin and superspin glasses are illustrated and contrasted. These properties are discussed in more detail in Case studies, taking into account the nanoparticle concentration, size and size distribution, using results from studies of ferrofluids and compacts of γ-Fe_2O_3 particles. The Outlook section illustrates recent findings suggesting that the temperature dependence of the low-field isothermal remanent magnetization (IRM) and magnetization as a function of magnetic field (hysteresis or M-H) curves of superspin glasses include information on the superspin dimensionality and magnetic anisotropy. The possibility to engineer nanocomposites with tailored magnetic interaction and anisotropy is also discussed.

3.1 Introduction

Interaction between particles in an ensemble of magnetic nanoparticles causes collective behaviour [1–5]. Figure 3.1 shows the temperature dependence of the zero-field-cooled (ZFC) and field-cooled (FC) magnetization of a dilute and a concentrated assembly of 8 nm maghemite nanoparticles prepared from the same batch. The magnetic response is altered by the dipolar interparticle interaction, yielding slowing down of the magnetization dynamics at low temperatures and a nonzero Weiss temperature (θ_w). The interparticle dipolar interaction transforms the nanoparticle system from being superparamagnetic to becoming a superspin glass (SSG). The

R. Mathieu (✉) · P. Nordblad
Department of Materials Science and Engineering, Uppsala University, Box 35, 751 03 Uppsala, Sweden
e-mail: roland.mathieu@angstrom.uu.se

D. Peddis et al. (eds.), *New Trends in Nanoparticle Magnetism*,
Springer Series in Materials Science 308,
https://doi.org/10.1007/978-3-030-60473-8_3

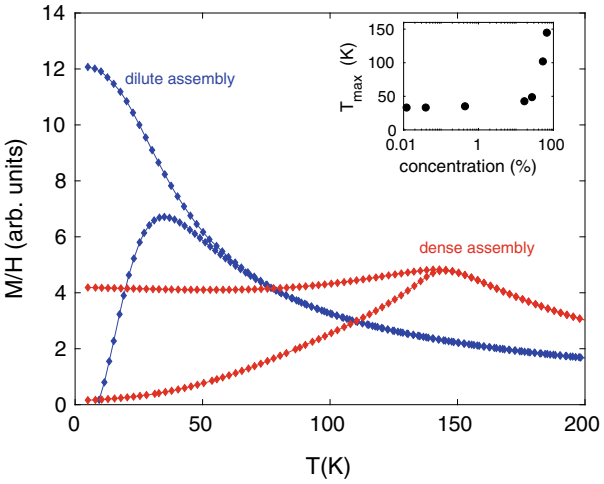

Fig. 3.1 Temperature dependence of the low-field ($H = 5$ Oe) ZFC and FC magnetization (M/H) of a dilute (blue) and a dense (red) assembly of 8 nm maghemite nanoparticles. The measured magnetization for the dense system has been corrected for demagnetization effects. The inset shows the variation of the temperature for the maximum in the ZFC curves ($T_{\max}$) as a function of particle concentration (logarithmic scale)

high-temperature behaviour follows the Curie–Weiss law: $\chi = C/(T-\theta_w)$, where C is assumed to be the same for the dilute and the dense system. The Weiss constant θ_w has from the measured data been derived to be about 90 K for the dense system and 0 K for the dilute system. There is thus a dominance of ferromagnetic interaction in the dense system.

3.1.1 Systems of Magnetic Nanoparticles

The magnetic behaviour of dilute (non-interacting) nanoparticle assemblies is governed by the sum of the response of each particle. The response of the individual particle depends on its magnetic moment ($m_{\rm sp}$) and its anisotropy ($E_{\rm ap}$). In an assembly of nanoparticles, there is a distribution of particle sizes and shapes and thus a corresponding distribution of $m_{\rm sp}(V)$ and $E_{\rm ap}(V)$ that is given by the composition and fabrication method of the particles. The building material of the particles can be ferromagnetic, ferrimagnetic or antiferromagnetic. The magnetic transition temperature of the particle material should be much higher than the temperatures where the magnetic properties of the particle system are studied.

3.1.2 Interaction Mechanisms

Dipolar interaction is always present and governed by the magnetic moment of the particles and the distance between particles. When the particles are touching, there is a possibility of direct or super-exchange interaction between particles. In a metallic matrix, interparticle interaction mediated via the conduction electrons becomes possible. If the matrix is antiferromagnetic, direct magnetic interaction at the interphase between matrix and particle occurs. Ferro- or ferrimagnetic matrices yield nanostructured magnets, which constitute a separate class of ordered magnetic materials. Figure 3.2 illustrates four different ways to suspend magnetic nanoparticles for physical property measurements. The two upper panels of Fig. 3.2 illustrate a ferrofluid, where the interparticle dipolar interaction is tuned by the concentration of particles and magnetic particles suspended in a matrix material. The matrix material can be a non-magnetic or an antiferromagnetic insulator or metal. In the two lower panels of Fig. 3.2, particles in the form of a powder or a compacted powder are illustrated. In these configurations, the interparticle distance can be tuned by the compacting pressure and the thickness of an insulating non-magnetic capping layer.

In the following, results obtained on compacts of γ-Fe_2O_3 maghemite, ferrofluids and nanocomposites, such as Fe nanoparticles embedded in Cr matrices, will be presented. The compacts will be referred to as "RCPx" (strongly interacting random closed-packed systems) and "REFx" (weakly interacting references), where "x" denotes the diameter of the constituting particles in nanometer [6]. Data obtained on spin glasses systems are included for comparison. Systems such as the Ag(11 at.%

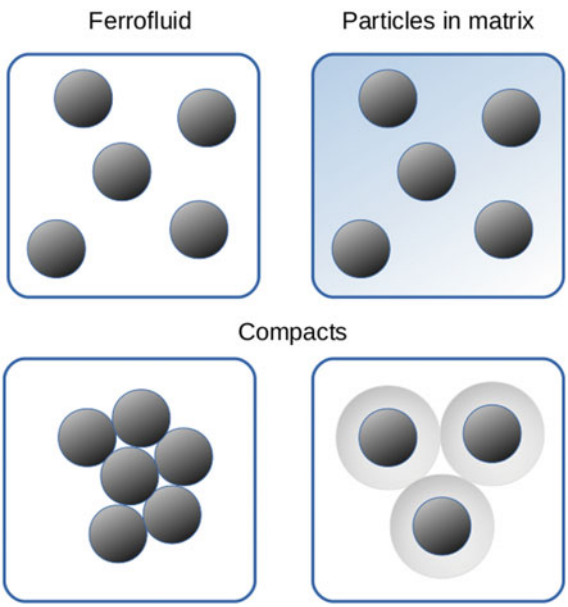

Fig. 3.2 Illustrations of magnetic particle assemblies: a ferrofluid (upper left), particles suspended in a solid matrix (upper right), bare compacted particles (lower left) and compacted particles with a capping layer (lower right)

Mn), Cu(13.5 at.% Mn) and Au(6 at.% Fe) will be referred to as Ag(Mn), Cu(Mn) and Au(Fe), respectively.

3.1.3 Time Scales

The dynamics of a magnetic nanoparticle is governed by the Arrhenius law $\tau_p = \tau_0 \exp(E_{\mathrm{ap}}/k_B T)$, where τ_{p} is the relaxation time of the particle, $\tau_0 \sim 10^{-11}$ s and k_B is the Boltzmann constant [7]. The thick black curve in Fig. 3.3 illustrates the evolution of the relaxation time of nanoparticles in an assembly of 8 nm maghemite particles (REF8) with quite narrow size distribution (using $E_{\mathrm{ap}} = \mathrm{KV}$ and $K \approx 50$ kJ/m^3) [8]. The corresponding data for smaller ($d = 7.5$ nm) and larger ($d = 8.5$ nm) particles is included using thin lines. The observation time (t_{obs}) range of conventional AC-susceptibility experiments is indicated by horizontal dashed lines ($t_{\mathrm{obs}} = 1/\omega$, where ω is the angular frequency of the AC-field). The particles become blocked when the relaxation time of the particles exceeds the observation time of the measurement. The distribution of particle sizes significantly broadens the region where blocking of the

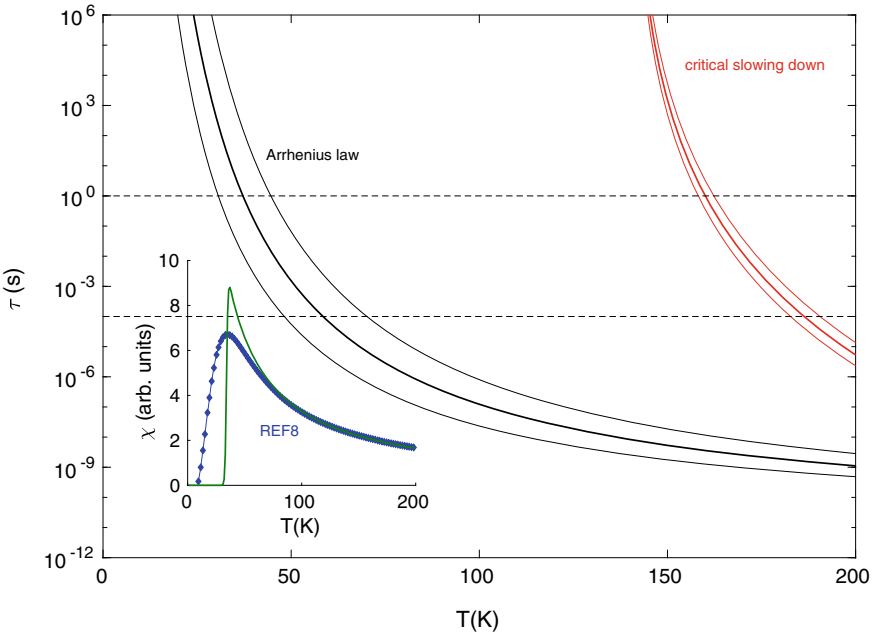

Fig. 3.3 Evolution of the particle relaxation time with temperature for dilute (grey) and dense (red) 7.5, 8 and 8.5 nm maghemite nanoparticles according to the Arrhenius law and assuming critical slowing down with $T_g = 140$ K, respectively. The inset shows the measured ZFC magnetization curve of REF8 and the calculated curve for a corresponding truly monodispersed 8 nm particle system

different particles occurs. The inset shows the measured low-field ZFC magnetization ($\chi = M/H$) of the dilute 8 nm assembly (REF8) and the calculated behaviour for a corresponding monodispersed 8 nm maghemite assembly (Debye AC susceptibility; $t_{obs} = 10$ s). Also drawn in Fig. 3.3 is the evolution of the relaxation time of the system assuming a compact nanoparticle system with dipolar interaction yielding $T_g = 140$ K. The individual particle relaxation time that corresponds to the volume of the particles and critical slowing down ($\tau_{crit} = \tau_p t^{-z\nu}$, $t = (T\text{-}T_g)/T_g$ [9] and $z\nu = 10$ the dynamic critical exponent) have been used to calculate the evolution of the critical relaxation time (τ_{crit}) of the dense particle assemblies (red curves; 7.5, 8 and 8.5 nm particles).

3.1.4 Model Behaviour Contra Collective Phenomena

A model superparamagnetic or superspin glass system would consist of monodispersed particles. However, such a system does not exist and the blocking behaviour of a non-interacting system of magnetic nanoparticles is always significantly broadened compared to a model calculation using the mean volume (see inset Fig. 3.3). The relaxation times of a model superspin glass approaching the glass temperature obey critical slowing down [10–13]. In spite of the inevitable size distribution of the nanoparticles, critical slowing down is observed in compact nanoparticle systems, with similar sharpness as that observed in archetypal atomic spin glasses [14]. On the other hand, nanoparticle systems with broader size distributions exhibit typical characteristics of collective dynamics in glassy magnetic systems such as ageing and memory phenomena although critical slowing down indicating a phase transition is not observed [15].

Figure 3.4 illustrates the correspondence between the ageing/memory behaviour of an archetypal spin glass (Cu(Mn)) [16] and a strongly interacting magnetic nanoparticle assembly (RCP8) showing superspin glass behaviour [6]. The main frames show low-field ZFC magnetization (M/H) versus temperature curves; a reference curve (red) where the system has been continuously cooled to a low temperature where the magnetic field is applied and the magnetization recorded on increasing temperature, and a memory curve (blue) where the sample has been kept at a halt temperature a wait time t_w during cooling. The memory curve shows a dip at the halt temperature as a memory of the halt [17]. The insets show ZFC magnetic relaxation at the halt temperatures using two different wait times (0 (red curves), and 3000 or 10,000 s (blue), respectively) at constant temperature before the magnetic field is applied. At an observation time of 100 s, the magnetization is lower when the system has been kept at constant temperature a longer wait time, this is in accord with the dip in the M versus T memory curves. The fact that the reference and memory M versus T curves coalesce at lower temperatures reflects the rejuvenation phenomenon (chaotic nature); the response of the (super)spin glass at lower temperatures is unaffected by the halt.

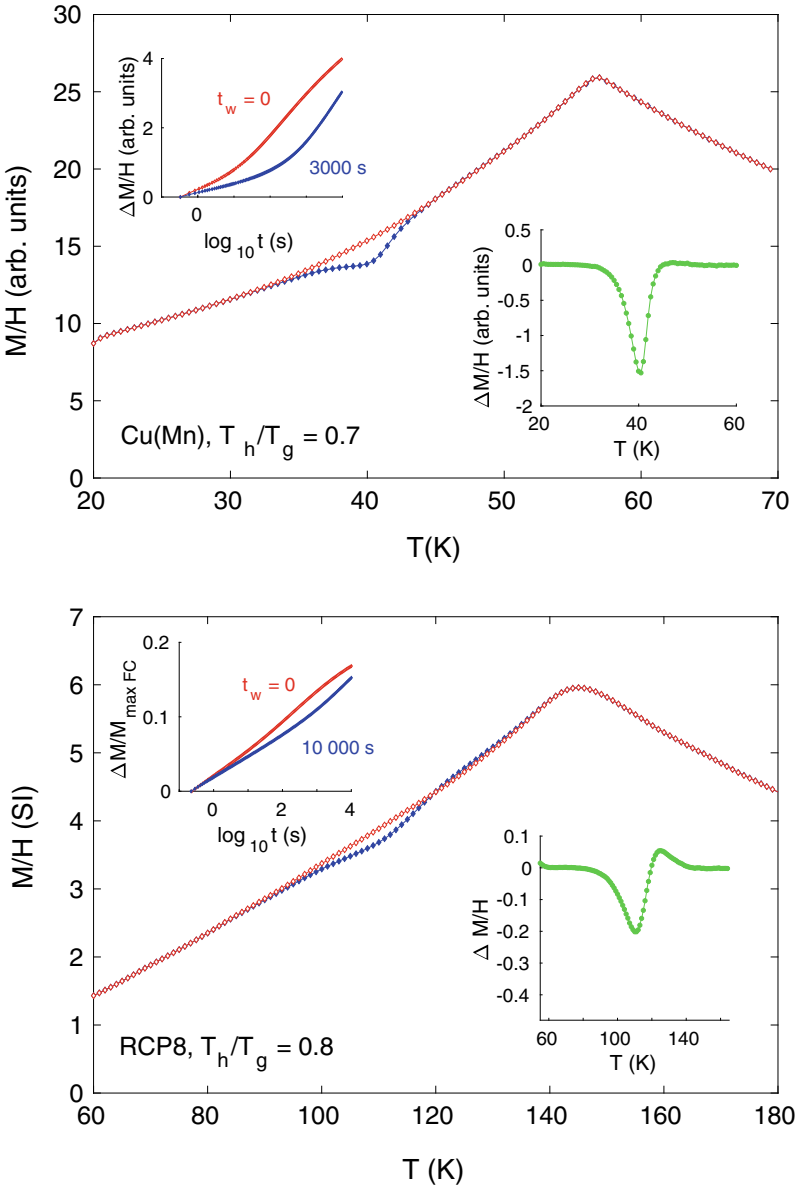

Fig. 3.4 M/H versus T (main frames) and M versus log (t) (upper insets) for an archetypal spin glass (top, Cu(Mn)) and a compacted ensemble of 8 nm maghemite nanoparticles (bottom, RCP8); $H =$ 0.5 Oe. In the latter case, corrections due to demagnetization effects have been made to extract the internal susceptibility. The main frames illustrate memory behaviour (lower insets show difference curves $\Delta M = M_{\text{mem}}$-$M_{\text{ref}}$) and the upper insets magnetization relaxation curves measured after two different wait times t_w as indicated in the figure

3.2 Case Studies: Superspin Glasses

Spin glasses are formed by atomic systems where there is structural disorder and competing ferro- and antiferromagnetic interaction giving rise to frustrated spins. The properties of model spin glasses such as Cu(Mn) and $Fe_{0.5}Mn_{0.5}TiO_3$ have been extensively studied and exhibit universal properties as to the existence of a second-order phase transition (revealed from static and dynamic scaling analyses) and infinite relaxation times and non-equilibrium dynamics manifested by ageing, memory and rejuvenation phenomena at temperature below T_g [18]. Measurable physical manifestations of superspin glass states are found in systems with strong enough dipolar interaction. Dipolar interaction can in randomly packed systems gives rise to dynamic frustration, i.e. depending on how neighbouring particles flip their magnetization direction, the dipolar moment on a specific particle changes sign with time. Strong enough means that the dipolar interaction strength causes a glass temperature that exceeds the blocking temperature (at the observation time (about 10 s) of magnetization versus temperature measurements) by a factor of two or more. For instance, if the dipolar interaction $E_{dd}/k_B = 100$ K, the anisotropy of the particles $E_{ap}/k_B < \log(\tau/\tau_{0)} \times T_B \sim 1250$ K (considering $T_B = 50$ K, on experimental observation time (10 s) and $\tau_0 = 10^{-11}$ s). Translated to observation times, this implies that the relaxation time of the particles at T_g, $\tau_p \sim 10^{-5}$ s. When T_g exceeds T_B by a factor of five, the relaxation time of the particles at T_g becomes $\tau_p \sim 10^{-9}$ s. To measure critical slowing down on the time scales of standard ac-susceptibility experiments (1–10,000 Hz, $t_{\text{obs}} = 1/\omega \sim 0.16$–$1.6 \times 10^{-5}$ s) the relaxation time of the slowest particles should always be much shorter than the observation time of the probe. In systems with weak interparticle interaction, this criterion is not fulfilled. On the other hand, as mentioned above (see Sect. 3.1.4), other manifestations of collective phenomena, such as ageing and memory, are readily observed in systems with wide distributions of particle sizes and comparably weak dipolar interparticle interaction.

3.2.1 Frozen Ferrofluids

Ferrofluids allow continuous tuning of the particle density and thus the strength of the interparticle dipolar interaction. Dense randomly packed frozen ferrofluids show magnetic ageing behaviour due to collective non-equilibrium dynamics introduced by dipolar dynamic frustration [14]. Interparticle interaction broadens the relaxation function at low temperatures and shifts the maximum in the low-field ZFC magnetization versus temperature curve to higher temperatures. In cases of strong dipolar interaction and narrow particle size distributions, critical slowing down indicating a spin glass like transition is observed on the time scales of AC-susceptibility experiments. An example of this is shown in Fig. 3.5 citing results from AC-susceptibility measurements on a system of FeC nanoparticles at different

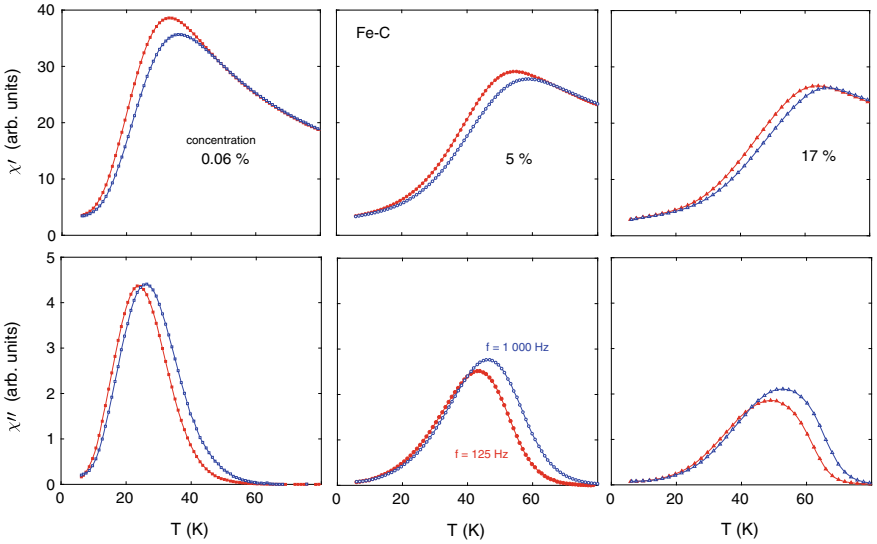

Fig. 3.5 In-phase (upper frame) and out-of-phase (lower frame) AC-susceptibility versus temperature at 125 Hz (red) and 1000 Hz (blue) for a frozen ferrofluid of amorphous Fe–C nanoparticles of different concentration; $h_{ac} = 0.1$ Oe. The figure is adapted from Fig. 3.1 in [10]

particle densities [10]. The sequence of curves elucidates the transformation of the particle assembly from superparamagnetic blocking behaviour to a superspin glass with increasing particle density and increased dipolar interaction strength. Analyses of the slowing down of the dynamics using wide frequency windows yield spin glass characteristic behaviour for the most dense sample, however with a microscopic relaxation time that corresponds the relaxation times of the particles near the derived glass temperature (T_g).

3.2.2 Compacts

Figure 3.1 showed ZFC-FC magnetization curves on assemblies of 8 nm maghemite nanoparticles with narrow size distribution (RCP8). The left panel of Fig. 3.6 shows the same ZFC/FC data for the compacted assembly together with the in- and out-of-phase components of the low-field AC-susceptibility measured at 10 Hz. The right panel shows the out-of-phase component of the AC-susceptibility data at different frequencies (0.17–510 Hz). The temperature for the onset of a finite out-of-phase component can be used as indicator of freezing of the magnetic moments on the time scale of that frequency. The dots near the onset indicate how the freezing temperatures (T_f) have been chosen for the different frequencies. Analysing the frequency dependence of the derived freezing temperatures according to critical slowing down, the best fit is found for $z\nu = 11$ and $\tau_p = 6 \times 10^{-12}$ s (see inset).

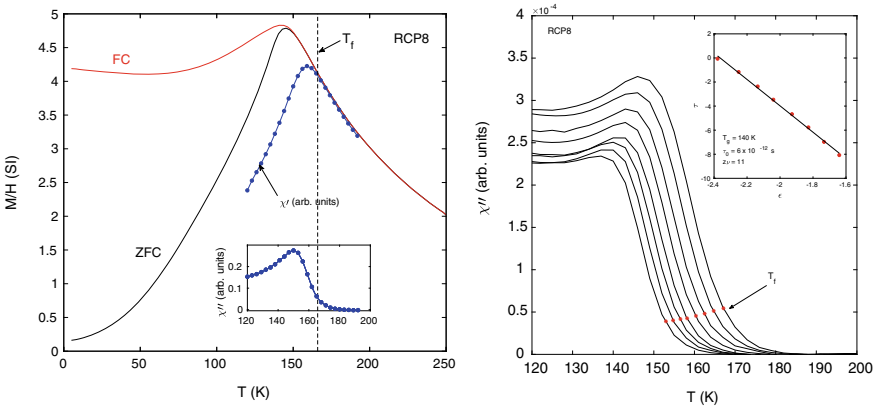

Fig. 3.6 DC and AC magnetic susceptibility versus temperature for RCP8. Left panel: ZFC and FC M/H ($H = 5$ Oe; corrected for demagnetizing effects) and $\chi'(T)$ and $\chi''(T)$ at 170 Hz ($h_{ac} = 4$ Oe). Right panel $\chi''(T)$ measured at 0.17–510 Hz and $h_{ac} = 4$ Oe. The inset shows the best fit of the data to critical slowing down

Corresponding systems of maghemite nanoparticles of other sizes have been investigated with the same experimental methods and found to exhibit critical slowing down [14]. Figure 3.7 shows the temperature dependence of the ZFC and FC magnetization (normalized to the magnetization value at the maximum of the ZFC curves) for compacted samples of sizes: 6, 8, 9 and 11.5 nm. The derived temperatures for the maximum in the ZFC magnetization versus temperature curves, T_{max}, are plotted as a function of particle volume in the inset together with the corresponding blocking temperatures for dilute samples of the same nanoparticles. The superspin glass temperatures derived from dynamic scaling analyses increase in a similar way

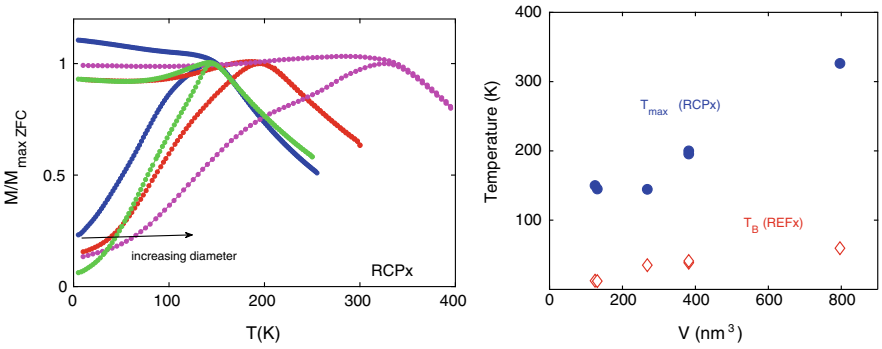

Fig. 3.7 Left panel: Normalized ZFC/FC magnetization versus temperature curves for compacted maghemite assemblies of 6, 8, 9 and 11.5 nm nanoparticles; $H = 5$ Oe. Right panel: T_{max} and T_B plotted versus the mean volume of the particles for the compact (RCP) and the dilute (REF) assemblies. The magnetization curves were not corrected for demagnetization effects [14, 20]

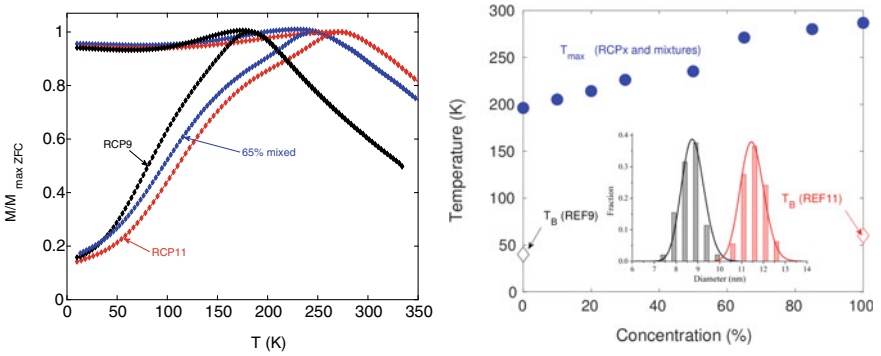

Fig. 3.8 Left panel: Normalized ZFC/FC magnetization versus temperature for compacted samples of 9 nm particles (RCP9), 11.5 nm particles (RCP11), and a mixture of 9 and 11.5 nm particles with 65% mixing fraction; $H = 5$ Oe. Right panel: $T_{\max}$ of the compacted mixed samples (RCP) versus concentration of large particles and T_B of the dilute 9 and 11.5 nm samples (REF9 and REF11, respectively). The inset shows the particle size distribution of the 9 and the 11.5 nm assemblies. The magnetization curves were not corrected for demagnetization effects [19, 20]

as $T_{\max}$ with particle volume. $T_{\max}$ (and T_g) exceeds T_B by a factor of 4 or more for all samples.

All the discussed compacted samples have similar and quite narrow particle size distributions and exhibit well-behaved critical slowing down indicating super-spin glass transitions [14]. Figure 3.8 shows ZFC and FC magnetization curves for compacted samples of 9 nm (RCP9) and 11.5 nm (RCP11) maghemite particles, as well as for a sample consisting of a mixture of 9 and 11.5 nm particles (65% mixing fraction). The volume ($2V$) of the 11.5 nm particles is about twice the volume (V) of the 9 nm particles. The size distributions of the two particle systems are shown as an inset in the right panel of Fig. 3.8. The evolution of the measured $T_{\max}$ with increasing fraction of larger particles is shown in the main frame of the right panel in Fig. 3.8. $T_{\max}$ increases linearly with the mixing fraction (mean particle size). Analyses of the frequency dependence of the freezing temperatures indicate that the assemblies of mixed particle sizes obey critical slowing down at all different mixing fractions from 0 to 100% of larger particles [19]. In all cases, the SSG temperature exceeds the blocking temperature of the dilute reference sample of the largest particles ($2V$) by at least a factor of three.

At low temperatures, where the particle moments are thermally blocked on the time scale of magnetization measurements, interparticle interaction can be revealed from a comparison between the field dependence of the isothermal remanent magnetization IRM(H) and the direct current demagnetization DCD(H) [21]. IRM is measured starting from a zero-field-cooled sample, applying a field pulse and then measuring the remanent magnetization M_{IRM} in zero field. DCD is measured starting from a high negative field ($-H_s$) that saturates the remanent magnetization (M_{RS}), applying a reversal field ($H_r \geq 0$), then removing this field and measuring the remanence M_{DCD} in zero field. The relative values of these remanences: $m_{IRM}(H) =$

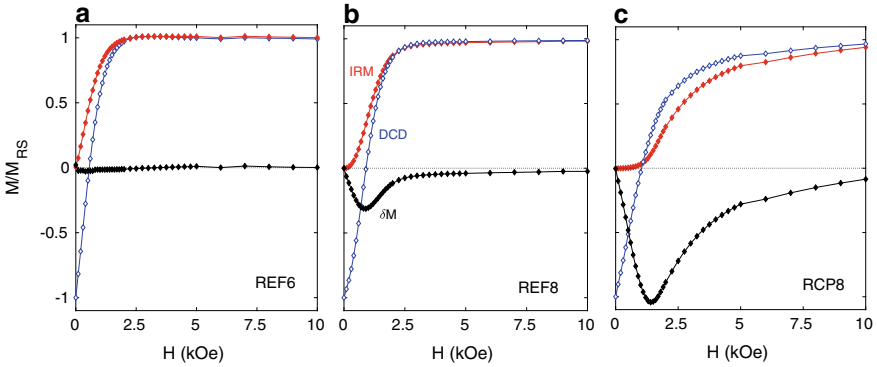

Fig. 3.9 m_{IRM}(H), m_{DCD}(H) and $\delta M(H)$ at $T = 5$ K for **a** non-interacting 6 nm particles **b** non-interacting 8 nm particles and **c** compact 8 nm particles [22]

$M_{\mathrm{IRM}}/M_{\mathrm{RS}}$, and $m_{\mathrm{DCD}}(H) = M_{\mathrm{DCD}}(H)/M_{\mathrm{RS}}$ are used to calculate $\delta M = m_{\mathrm{DCD}}$-(1–$2m_{\mathrm{IRM}}$). For a non-interacting system of ideal superspins $\delta M = 0$ at all fields, whereas for systems with interparticle interaction and/or non-ideal particle moments $\delta M(H) \neq 0$ at low fields [21]. The field dependences of IRM, DCD and δM of REF6, REF8 and RCP8 at 5 K are shown in Fig. 3.9 a–c. REF6 shows the expected behaviour of a non-interacting system of magnetic nanoparticles being switched according to the Stoner–Wohlfarth model, i.e. $\delta M(H) \approx 0$ at all fields. For REF8 on the other hand, $\delta M(H) \neq 0$ at low fields. The different behaviour of REF6 and REF8 reflects non-ideal behaviour of the 8 nm particles [22]; these particles exhibit finite exchange bias after field cooling, whereas the 6 nm particles do not. Figure 3.9c shows the very strong influence that interparticle interaction and collective behaviour of the compact 8 nm particle system (RCP8) has on the field dependence of δM.

At higher temperatures, thermal relaxation implies that the measures M_{IRM}, M_{DCD} and δM become time dependent: i.e. dependent on the duration of the magnetic field pulse (how long time H_r has been applied), the observation time of the measurement of the remanence and for an interacting system the wait time before the magnetic field is applied after zero-field cooling. This implies that also these time parameters need to be controlled when this kind of measurements is made at temperatures where significant magnetic relaxation occurs. The crucial influence that thermal relaxation has on the hysteresis behaviour of (super)spin and glasses is evidenced by first-order reversal curves (FORC) simulations of an Edwards-Anderson Ising spin glass at $T = 0$ and $T = 0.3\ T_g$, where finite temperature smoothens all sharp features of the FORC diagram (in accord with experimental results) and effectively wipes out the reversal field memory effect characteristic of 3D Ising spin glasses at $T = 0$ K [23]. FORC diagrams and magnetic hysteresis of Heisenberg spin glasses are on the other hand dominated by an induced excess moment that exhibits field-dependent exchange bias [24, 25]. FORC diagrams of RCP8 at low temperature are very different from those of the weakly interacting system (which primarily are controlled by the particle size distribution) but also very different from FORCs of atomic spin glasses [22].

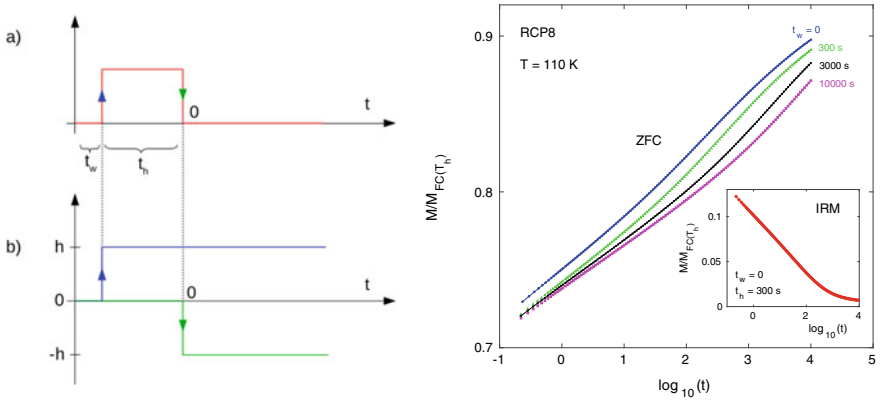

Fig. 3.10 Left: Equivalent field change sequence for a field pulse of duration t_h. Right: M_{ZFC} (t_w, t)/M_{FC} versus log(t) recorded in $H = 0.5$ Oe and calculated $m_{\mathrm{IRM}}(t)$ for RCP8 ($t_w = 0$)

At low fields, where the particle system obeys linear response to field applications, M_{IRM} reflects the relaxation function, $p(t_w, t)$ and the time dependence of $M_{\mathrm{IRM}}(t)$ obeys the principle of superposition. The relaxation function is directly measured by the ZFC relaxation after the application of a weak magnetic field (h): $p(t_w, t) = M_{\mathrm{ZFC}}(t_w, t)/h$ [26], where t is the time elapsed after the field application and t_w the wait time at constant field before the magnetic field is applied. The right panel of Fig. 3.10 shows zero-field-cooled magnetic relaxation, $M_{\mathrm{ZFC}}(t, t_w)$ versus log (t), of the compact 8 nm particle assembly (RCP8) measured at 110 K. The relaxation at temperatures below T_g (= 140 K) occurs over extended time scales stating from the individual particle relaxation time (τ_p) and continuing well beyond any experimental time scales.

The fact that there is a wait time dependence of the relaxation function implies that the system experiences magnetic ageing, as already the memory behaviour suggested (Fig. 3.4). The magnitude of the low-field IRM is controlled by the relaxation function $p(t_w, t)$: and given by: $M_{\mathrm{IRM}}(t) = hp(tw, t + t_h) - hp(t_w + t_h, t)$ [26]. Where the response function empirically is defined from the measured $M_{\mathrm{ZFC}}(t_w, \mathrm{t})$ curves. The inset of the right panel of Fig. 3.10 shows the calculated m_{IRM}(t) using the $t_w = 0$ and $t_w = 300$ s curves of the main panel and the field application sequence is indicated in the left panel of Fig. 3.10: a positive field is applied at $t = 0$ and a negative field change h (= 0.5 Oe) is made at time t_h (= 300 s). The remanence, m_{IRM} [$= M_{\mathrm{IRM}}/M_{\mathrm{FC}}(T_h)$], that has been attained after the field has been cut to zero can be frozen in by immediately cooling the sample to lower temperatures. Figure 3.11 shows the temperature dependence of M_{IRM} on cooling and heating (red dots) and on heating after the sample has been quenched to low temperature immediately after the field has been switched off (black dots) [27]. As can be seen by the red curve there is a rapid decrease of the magnetization in the temperature region close to the halt temperature (cf. the decay of $m_{\mathrm{IRM}}(t)$ on a linear scale shown in the inset of Fig. 3.11, the same m_{IRM} data as shown on a logarithmic scale in

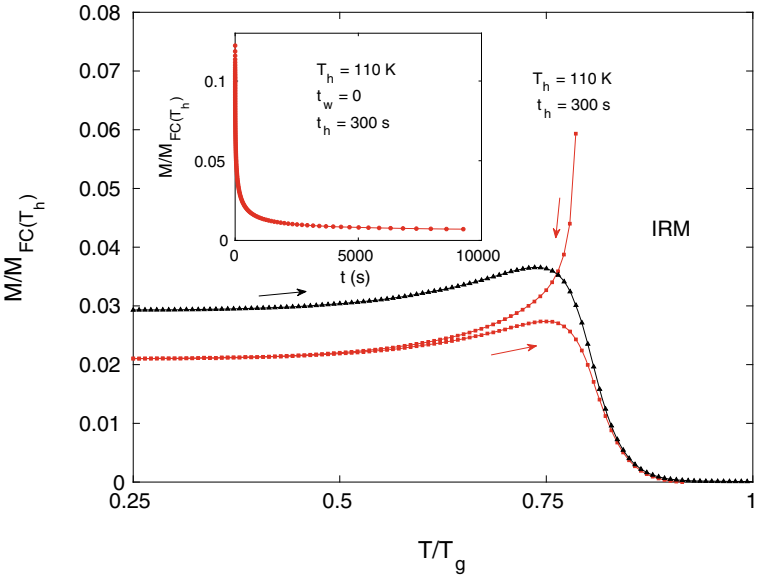

Fig. 3.11 $m_{\mathrm{IRM}}(T)$ measured on cooling and subsequent heating (red curves) and on heating after rapid cooling to low temperatures (black curve) (RCP8, $h = 0.5$ Oe). Inset: calculated $m_{\mathrm{IRM}}(t)$ for RCP 8 ($t_w = 0$) from Fig. 3.10 (linear scale)

Fig. 3.10). $m_{\mathrm{IRM}}(T)$ very rapidly decays towards zero when the temperature reaches near the temperature where it was attained. The frozen in magnetization attained in the time window 1–300 s rapidly relaxes when their relaxation times again reaches the order of the observation time of the magnetization measurement (~10 s).

3.3 Outlook

3.3.1 Superspin Dimensionality

Experiments on different spin glasses have shown that the frozen in $m_{\mathrm{IRM}}(T)$ can be used as an indicator of the spin dimensionality of the investigated spin glass [28]. The inset of the left panel of Fig. 3.12 shows the temperature dependence of m_{IRM} of an Ising and a Heisenberg spin glass as a function of T/T_g, where m_{IRM} has been frozen in at $T_h/T_g = 0.6$. There is a clear distinction between the behaviour of the two systems near T_h: the curve for the Ising spin glass smoothly decays whereas $m_{\mathrm{IRM}}(T)$ of the Heisenberg system exhibits a distinct maximum before decaying towards zero. The right panel of Fig. 3.12 shows corresponding curves for a compact of 8 nm maghemite particles (RCP8) with a superspin glass temperature of 140 K. Notable in the figure is that the low-temperature curves show a smooth decay of $m_{\mathrm{IRM}}(T)$ (Ising like)

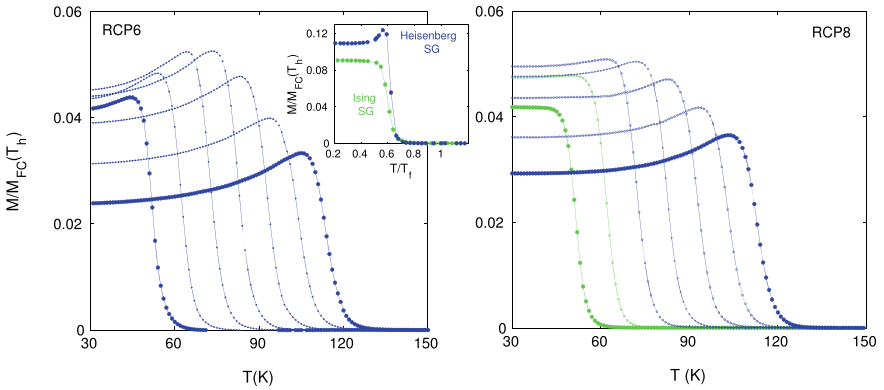

Fig. 3.12 Superspin dimensionality and relation to T_B for RCP6 and RCP8 (T_g ~ 140 K in both cases). $m_{\mathrm{IRM}}(T)$ is recorded on reheating after halts made at $T_h = 50$, 60, 70, 80, 90, 100 and 110 K ($h = 0.5$ Oe, $t_h = 300$ s) during the cooling. The inset shows $m_{\mathrm{IRM}}(T)$ for Ising and Heisenberg spin glasses, for T_h/T_g ~ 0.6–0.7 ($h = 10$ Oe, $t_h = 3000$ s) [28]

at lower temperatures, whereas the curves at higher temperatures exhibit a clear maximum (Heisenberg like) before the decay. All $m_{\mathrm{IRM}}(T)$ curves for the compact of 6 nm particles on the other hand exhibit a clear maximum (Heisenberg like) before rapidly decaying to zero at temperatures above T_h. The significant dynamic difference between the two systems is that the blocking temperatures of the non-interacting systems are significantly different although the superspin glass temperatures are the same (140 K) for the two compacts. $T_B = 12.5$ K for the non-interacting system 6 nm particles and $T_B = 35$ K for the compact 8 nm particle assembly. This difference between the two compacts hints that the crossover is related to the evolution of the relaxation times of the particles with temperature and that the particles behave Ising like at temperatures $T < T_B$ and Heisenberg like at $T \gg T_B$. At low temperatures, the particles are mainly confined to point along the anisotropy direction, whereas at higher temperature, $T \gg T_B$, they very rapidly switch between the two energy minima. This type of experiments reflects properties of the collective dynamics of the particle system and is only viable in the temperature region between T_B and T_g. At temperatures below T_B of the non-interacting system, the particles are essentially blocked on the time scales of the experiment and no remanence is induced from a field pulse of duration minutes.

The spin dimensionality has been found to affect the anisotropy and reversal of the magnetization of spin glasses [25]. For example strikingly different hysteresis curves are displayed by spin glasses such as Au(Fe) with an Ising character—brought forth by the single ion anisotropy of the Fe spins—and the above-discussed Cu(Mn) Heisenberg spin glass. As seen in Fig. 3.13 (main frames), the ZFC M(H) curves of the Heisenberg system include an excess moment (ΔM). Furthermore, as seen in inset, these curves, like the field-cooled ones recorded after cooling the system in H_{FC}, are exchange biased. The FC $M(H)$ data recorded after sweeping the magnetic field from H_{FC} to $-H_{FC}$ and back includes an excess moment and defines two switching fields.

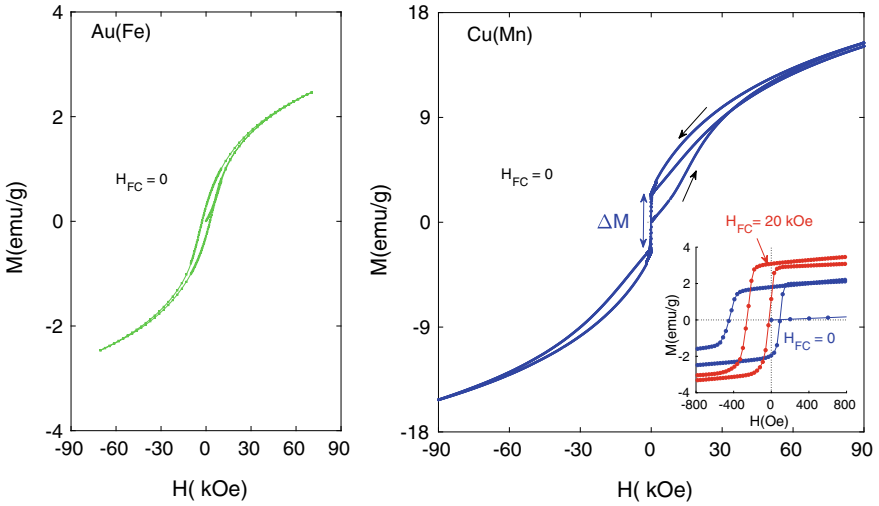

Fig. 3.13 Zero-field-cooled M(H) hysteresis loops at low temperatures ($T/T_g \sim 0.08$) for two spin glasses with Ising (Au(Fe), $T_g = 24$ K) and Heisenberg (Cu(Mn), $T_g = 57$ K) characters. The inset shows the zero-field-cooled and field-cooled ($H_{\mathrm{FC}} = 20$ kOe) on a smaller field scale for the Cu(Mn) spin glass; adapted from [29]

This behaviour has been interpreted in term of the chirality of the spin structure of Heisenberg systems, which may be affected by a small magnetic field applied during cooling, and the excess moment ΔM.

This brings forth unidirectional and uniaxial anisotropies and their respective switching fields [25]. The evolution of $m_{\mathrm{IRM}}(T)$ curves with T_h presented in Fig. 3.12, and the behaviour of FORC distributions for superspin glasses [22] suggest that such $M(H)$ experiments shall be relevant to superspin glasses.

3.3.2 Nanocomposites

Magnetic nanoparticles covered with an antiferromagnetic shell or dispersed in an AF-matrix have magnetic properties that emanate from direct exchange coupling at the interphase between the ferro- or ferrimagnetic core of the particles and the AF-coating/matrix. Unidirectional anisotropy and shifted FC hysteresis loops (exchange bias) were reported by Meiklejohn and Bean [30] in the mid 1950ies: "The material that exhibits this property is a compact of fine particles of Co (100–1000 Å) that have a cobaltous oxide coating". This phenomenon is illustrated in Fig. 3.14 which shows low-temperature hysteresis curve recorded after zero-field cooling and field cooling for amorphous Fe@(Fe,O) core-shell nanoparticles (core diameter ~8 nm, shell thickness ~2 nm). In the latter case, the $M(H)$ curve is recorded by increasing the magnetic field strength from its cooling value H_{FC} to the maximum ($H_{\mathrm{max}} = 50$ kOe),

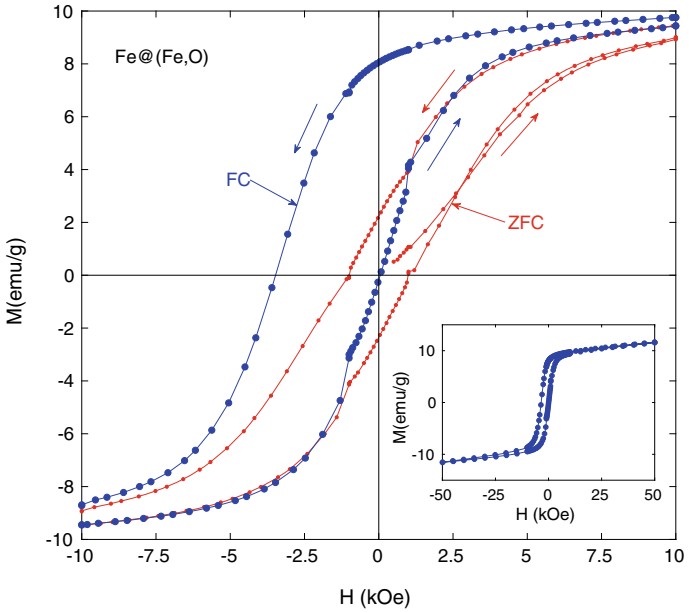

Fig. 3.14 Low-temperature hysteresis curves for a system of Fe@(Fe, O) core-shell nanoparticles recorded under zero-field-cooled and field-cooled ($H_{FC} = 10$ kOe) conditions. The inset shows a complete ZFC M(H) curve measured up to ± 5 T; adapted from [31]

and then cycling the magnetic field to $\pm H_{max}$ [31]. Some decades after Meiklejohn and Bean's discovery, in 2003, a corresponding system of Co nanoparticles with a Co core of 30–40 Å and a shell of CoO of about 10 nm was found "Beating the superparamagnetic limit with exchange bias" [32]. These particles were investigated embedded in a paramagnetic (Al_2O_3), as a compacted powder and embedded in an antiferromagnetic CoO matrix. The behaviour is remarkably different in between the three systems and indicates that the particles in Al_2O_3 behave as a superparamagnetic system with thermally blocked particles at temperatures below 10 K. When embedded in an antiferromagnetic CoO matrix, the particles become exchange coupled to the matrix and blocked up to the Neel temperature of CoO near room temperature [32]. In addition, the low-temperature FC hysteresis loops of the CoO embedded particles are strongly exchange biased, in accord with the Meiklejohn and Bean findings.

It was reported recently that including the Co@CoO core-shell particles in a Cu_2O matrix would enhance the interfacial morphology and exchange bias [33]. Interestingly, the matrix may have specific electrical and magnetic properties, which affect the magnetic interaction as well as exchange bias of the embedded particles. For example small (~2 nm diameter) Co nanoparticles embedded in a Mn matrix were found to interact magnetically, while the same particles in a Ag matrix show little interaction effects [34, 35].

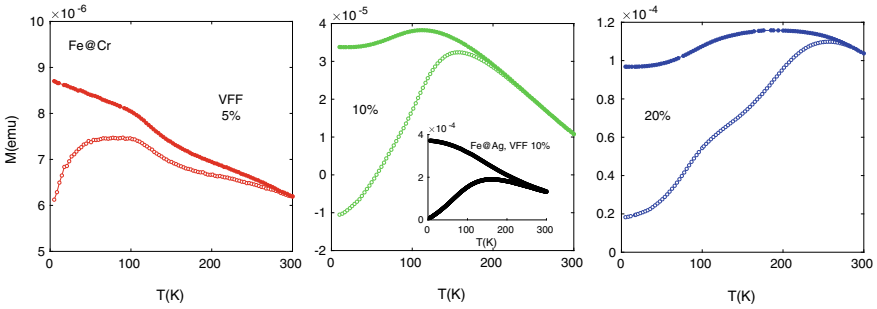

Fig. 3.15 ZFC/FC magnetization for Fe@Cr nanocomposites, consisting of 2 nm Fe particles embedded in a Cr matrix, with volume filling fraction (VFF) of 5, 10 and 20% ($H = 10$ Oe). The inset shows the corresponding magnetization curve for similar particles embedded in a non-magnetic Ag matrix (Fe@Ag) [36]

In the related system of similarly small Fe particles embedded in a Cr matrix, the magnetic anisotropy and interparticle interaction of the particles are greatly influenced by the Cr matrix [36]. As illustrated by the middle panel of Fig. 3.15, the magnetization curves of the Fe@Cr nanocomposite with a volume filling fraction of 10% are reminiscent to those superspin glasses (main frame). On the other hand, the Fe@Ag nanocomposite with the same filling fraction exhibits a superparamagnetic-like behaviour with a lower blocking temperature [36]. The evolution of the magnetization curves in Fig. 3.13 mimics those of the susceptibility curves depicted in Fig. 3.5 for a ferrofluid with increasing particle concentration. In the present case, a ferromagnetic-like response is observed for the largest volume filling fractions [2]. One could envisage that inversed magnetic nanoparticle systems such as non-magnetic nanoparticles (holes) in an antiferromagnetic matrix may provide collectively locked field-cooled excess moments with extraordinary high coercivity and paramagnetic zero-field-cooled behaviour.

Nanocomposites comprising two or more materials mixed on the nanoscale may be designed, in order to maximize the interaction between the two constituents. For example exchange-spring nanocomposites have been considered as a novel way to design permanent magnets [37, 38]. In spintronic nanocomposites including transition metal oxides, it was found that magnetoresistive [39] and magnetoelectric [40] properties could be tuned owing to the interaction of the two constituting phases. Hole-doped $La_{1-x}Ca_xMnO_3$ transition metal oxides (x is the hole concentration) are prototypical colossal magnetoresistance manganites [41]. Akin to the results of [39], it is expected that in nanocomposites of $La_{0.67}Ca_{0.33}MnO_3$ (LCMO) and $CoFe_2O_4$ (CFO), $CoFe_2O_4$ particles may exert a dipolar field onto the LCMO ones. Two types of composites have been considered, either the simple mechanical mixture (nanomixture) of the two nanosystems, or LCMO nanoparticles grown around the CFO ones (nanocomposite) [42]. Interestingly in this case, the CFO phase acts as hard phase for the soft LCMO. As seen in Fig. 3.16, owing to the more homogeneous core-shell-like morphology in the nanocomposite, interaction of the two phases is much

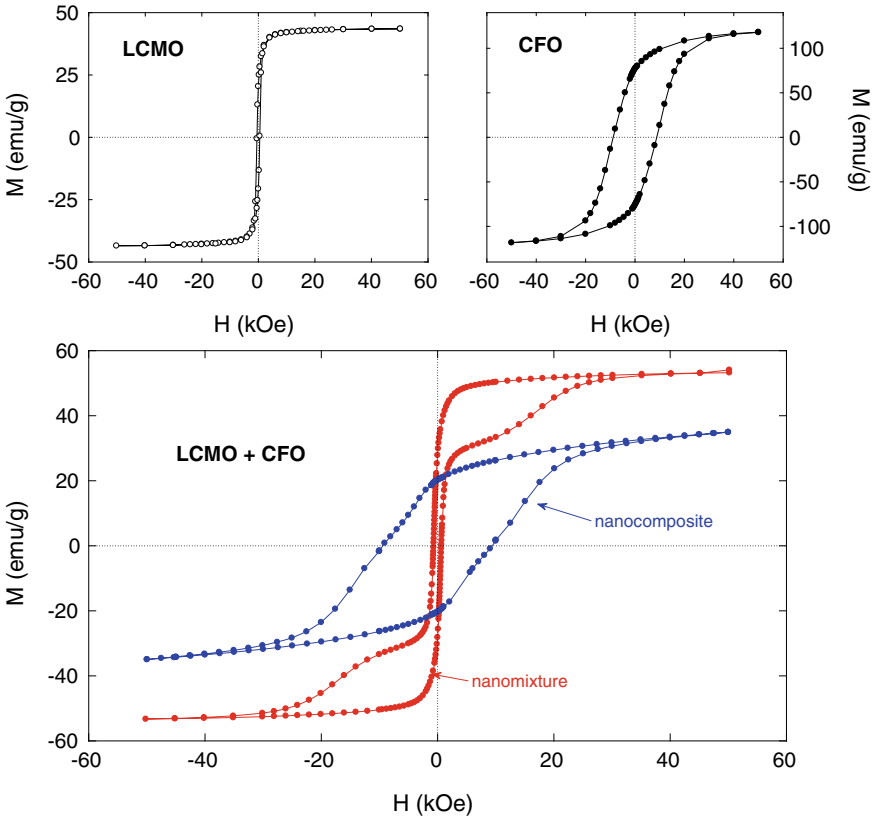

Fig. 3.16 Low-temperature M(H) hysteresis curves for (top panels) $La_{0.67}Ca_{0.33}MnO_3$ (LCMO) and $CoFe_2O_4$ (CFO), and (bottom panels) composite nanosystems (LCMO + CFO) [42]

stronger and switching is more coherent, akin to that observed in exchange-coupled nanocomposites [37, 38]. On the other hand, the M(H) curves of the nanomixture show two individual switchings, corresponding to the independent switching of the two phases. Interestingly, there are many parameters which may be varied to tune the magnetic (e.g. electrical) properties of such exchange-spring-like nanocomposites, for example phase volume fractions, magnetic properties (saturation magnetization, anisotropy) of the phases, and particles size.

3.3.3 Superstructures

The magnetic nanoparticle systems that we have discussed are all amorphous from a structural point of view, i.e. the particles are randomly distributed in space. Assemblies of nanoparticles are found to display magnetic properties determined by the

arrangements of the particles and orientational dependence of the magnetic interaction [43]. The organization of the particles results in the formation of three-dimensional structures, such as helices [44], superlattices [45], and other nanostructures [46] and mesoscopic systems [47, 48]. Systems built on spatial structural order provide possibilities of ordered magnetic structures. The fabrication and study of superferromagnets, superferrimagnets and superantiferromagnets provide a challenging field of collective experimental magnetism promoted by the possibility of 3D printing on the mesoscale [49].

Acknowledgements The authors are grateful to all their co-workers. This chapter includes results obtained in collaboration with M. S. Andersson, G. Muscas, P. Anil Kumar, M. Hudl, as well as D. Peddis, G. Singh, J. A. de Toro and their respective groups. The Swedish Research Council (VR) is thanked for financial support.

References

1. P. Jönsson, Adv. Chem. Phys. **128**, 191–248 (2004)
2. S. Bedanta, W. Kleemann, J. Phys. D Appl. Phys. **42**, 013001 (2009)
3. S. Mörup, M.F. Hansen, C. Frandsen, Beilstein J. Nanotechnol. **1**, 182–190 (2010)
4. S. Bedanta, O. Petracic, W. Kleemann, Supermagnetism in *Handbook of Magnetic Materials 23*, ed. by K. H. J. Buschow (Elsevier, 2017), pp. 1–83
5. D.S. Schmool, H. Kachkachi, Collective effects in assemblies of magnetic nanoparticles. in *Solid State Physics 67*, ed. by R.E. Camley, R.L. Stamps (Academic Press, 2016), pp. 1–97
6. J.A. De Toro, S.S. Lee, D. Salazar, J.L. Cheong, P.S. Normile, P. Muniz, J.M. Riveiro, M. Hillenkamp, F. Tournus, A. Tamion, P. Nordblad, Appl. Phys. Lett. **102**, 183104 (2013)
7. D.L. Leslie-Pelecki, R.D. Rieke, Chem. Mater. **8**, 1770 (1996)
8. M.S. Andersson, J.A. De Toro, S.S. Lee, P.S. Normile, P. Nordblad, R. Mathieu, Phys. Rev. B **93**, 054407 (2016)
9. K. Binder, A.P. Young, Rev. Mod. Phys. **58**, 801 (1986)
10. M.F. Hansen, P.E. Jönsson, P. Nordblad, P. Svedlindh, J. Phys. Condens. Matter **14**, 4901–4914 (2002)
11. C. Djurberg, P. Svedlindh, P. Nordblad, M.F. Hansen, F. Bödker, S. Mörup, Phys. Rev. Lett. **79**, 5154–5157 (1997)
12. J.L. Dormann, R. Cherkaoui, L. Spinu, M. Nogues, F. Lucari, F. D'Orazio, D. Fiorani, A. Garcia, E. Tronc, J.P. Jolivet, J. Magn. Magn. Mater. **187**, L139–L144 (1998)
13. K. Hiroi, K. Komatsu, T. Sato, Phys. Rev. B **83**, 224423 (2011)
14. M.S. Andersson, R. Mathieu, P.S. Normile, S.S. Lee, G. Singh, P. Nordblad, J.A. De Toro, Mater. Res. Express **3**, 045015 (2016)
15. T. Jonsson, J. Mattsson, C. Djurberg, F.A. Khan, P. Nordblad, P. Svedlindh, Phys. Rev. Lett. **75**, 4138 (1995)
16. R. Mathieu, M. Hudl, P. Nordblad, Europhys. Lett. **90**, 67003 (2010)
17. R. Mathieu, P. Jönsson, D.N.H. Nam, P. Nordblad, Phys. Rev. B **63**, 092401 (2001)
18. P.E. Jönsson, R. Mathieu, P. Nordblad, H. Yoshino, H. Aruga Katori, A. Ito, Phys. Rev. B **70**, 174402 (2004)
19. M.S. Andersson, R. Mathieu, P.S. Normile, S.S. Lee, G. Singh, P. Nordblad, J.A. De Toro, Phys. Rev. B **95**, 184431 (2017)
20. P.S. Normile, M.S. Andersson, R. Mathieu, S.S. Lee, G. Singh, J.A. De Toro, Appl. Phys. Lett. **109**, 152404 (2016)

21. J. García-Otero, M. Porto, J. Rivas, J. Appl. Phys. **87**, 7376–7381 (2000)
22. J.A. De Toro, M. Vasilakaki, S.S. Lee, M.S. Andersson, P.S. Normile, N. Yaacoub, P. Murray, E.H. Sanchez, P. Muniz, D. Peddis, R. Mathieu, K. Liu, J. Geshev, K.N. Trohidou, J. Nogues, Chem. Mater. **29**, 8258 (2017)
23. H. G. Katzgraber, D. Hérisson, M. Östh, P. Nordblad, A. Ito, H. Aruga Katori, Phys. Rev. B **76**, 092408 (2007)
24. M. Östh, D. Hérisson, P. Nordblad, J. Magn. Magn. Mater. **310**, e525–e527 (2007)
25. M. Hudl, R. Mathieu, P. Nordblad, Sci. Rep. **6**, 19964 (2016)
26. L. Lundgren, P. Nordblad, L. Sandlund, Europhys. Lett. **1**, 529–534 (1986)
27. M.S. Andersson, J.A. de Toro, S.S. Lee, R. Mathieu, P. Nordblad, Europhys. Lett. **108**, 17004 (2014)
28. R. Mathieu, M. Hudl, P. Nordblad, Y. Tokunaga, Y. Kaneko, Y. Tokura, H. Aruga Katori, A. Ito, Philos. Mag. Lett. **90**, 723 (2010)
29. P. Nordblad, M. Hudl and R. Mathieu, Exchange bias in dilute magnetic alloys in *Exchange Bias: From Thin Film to Nanogranular and Bulk Systems*, ed. by S.K. Sharma (CRC Press, 2017) p 71
30. W.H. Meiklejohn, C.P. Bean, Phys. Rev. **102**, 1413–1414 (1956); ibidem **105**, 904–913 (1957)
31. P. Anil Kumar, G. Singh, W.R. Glomm, D. Peddis, E. Wahlström, R. Mathieu, Mater. Res. Express **1**, 036103 (2014)
32. V. Skumryev, S. Stoyanov, Y. Zhang, G. Hadjipanayis, D. Givord, J. Nogués, Nature **423**, 850–853 (2003)
33. J.A. González, J.P. Andrés, R. López Antón, J.A. De Toro, P.S. Normile, P. Muniz, J.M. Riveiro, J. Nogués, Chem. Mater. **29**, 5200–5206 (2017)
34. N. Domingo, D. Fiorani, A.M. Testa, C. Binns, S. Baker, J. Tejada, J. Phys. D Appl. Phys. **41**, 134009 (2008)
35. G. Margaris, M. Vasilakaki, D. Peddis, K.N. Trohidou, S. Laureti, C. Binns, E. Agostinelli, D. Rinaldi, R. Mathieu, D. Fiorani, Nanotechnology **28**, 035701 (2017)
36. D. Peddis, M.T. Qureshi, S.H. Baker, C. Binns, M. Roy, S. Laureti, D. Fiorani, P. Nordblad, R. Mathieu, Philos. Mag. **95**, 3798 (2015)
37. H. Zeng, J. Li, J.P. Liu, Z.L. Wang, S. Sun, Nature **420**, 395 (2002)
38. B. Balamurugan, D.J. Sellmyer, G.C. Hadjipanayis, R. Skomski, Scripta Mater. **67**, 542–547 (2012)
39. P. Anil Kumar, D.D. Sarma, Appl. Phys. Lett. **100**, 262407 (2012)
40. H. Zheng, J. Wang, S.E. Lofland, Z. Ma, L. Mohaddes-Ardabili, T. Zhao, L. Salamanca-Riba, S.R. Shinde, S.B. Ogale, F. Bai, D. Viehland, Y. Jia, D.G. Schlom, M. Wuttig, A. Roytburd, R. Ramesh, Science **303**, 661–663 (2004)
41. Y. Tokura, N. Nagaosa, Science **288**, 462 (2000)
42. G. Muscas, P. Anil Kumar, G. Barucca, G. Concas, G. Varvaro, R. Mathieu, D. Peddis, Nanoscale **8**, 2081 (2016)
43. D. Peddis, C. Cannas, A. Musinu, A. Ardu, F. Orrù, D. Fiorani, S. Laureti, D. Rinaldi, G. Muscas, G. Concas, G. Piccaluga, Chem. Mater. **25**, 2005–2013 (2013)
44. G. Singh, H. Chan, A. Baskin, E. Gelman, N. Repnin, P. Král, R. Klajn, Science **345**, 1149–1153 (2014)
45. J. Chen, A. Dong, J. Cai, X. Ye, Y. Kang, J.M. Kikkawa, C.B. Murray, Nano Lett. **10**, 5103–5108 (2010)
46. G. Singh, H. Chan, T. Udayabhaskararao, E. Gelman, D. Peddis, A. Baskin, G. Leitus, P. Král, Rafal Klajn, Faraday Discuss. **181**, 403 (2015)
47. A. Fabian, M.T. Elm, D.M. Hofmann, P.J. Klar, J. Appl. Phys. **121**, 224303 (2017)
48. Elena V. Sturm, Helmut Cölfen, Crystals **7**, 207 (2017)
49. M.S. Saleh, C. Hu, R. Panat, Sci. Adv. **3**, e1601986 (2017)